

Large-eddy simulation of traffic-related air pollution at a very high-resolution in a mega-city: Evaluation against mobile sensors and insights for influencing factors

5 Yanxu Zhang¹, Xingpei Ye¹, Shibao Wang¹, Xiaojing He², Lingyao Dong¹, Ning Zhang¹,
Haikun Wang¹, Zhongrui Wang¹, Yun Ma¹, Lei Wang¹, Xuguang Chi¹, Aijun Ding¹,
Mingzhi Yao³, Yunpeng Li³, Qilin Li³, Ling Zhang⁴, Yongle Xiao⁴

¹School of Atmospheric Sciences, Nanjing University, Nanjing, China

10 ²School of Environment, Nanjing University, Nanjing, China

³Beijing SPC Environment Protection Tech Company Ltd., Beijing, China

⁴Hebei Saihero Environmental Protection Hi-tech. Company Ltd., Shijiazhuang, Hebei, China

Correspondence to: Yanxu Zhang (zhangyx@nju.edu.cn), Ning Zhang (ningzhang@nju.edu.cn), and
Haikun Wang (wanghk@nju.edu.cn)

15

Abstract. Urban air pollution has tremendous spatial variability at scales ranged from kilometer to meters due to unevenly distributed emission sources, complex flow patterns, and photochemical reactions. However, high-resolution air quality information is not available through traditional approaches such as ground-based measurements and regional air quality models (with typical resolution >1 km). Here we develop a ten-meter resolution air quality model for traffic-related CO pollution based on the parallelized large-eddy simulation model (PALM). The model performance is evaluated with measurements obtained from sensors deployed on a taxi platform, which collects data with a comparable spatial resolution to our model. The very high resolution of the model reveals a detailed geographical dispersion pattern of air pollution in and out of the road network. The model results ($0.92 \pm 0.40 \text{ mg/m}^3$) agree well with the measurements ($0.90 \pm 0.58 \text{ mg/m}^3$, $n = 114,502$). The model has similar spatial patterns with that of the measurements, and the r^2 value of a linear regression between model and measurement data is 0.50 ± 0.07 during non-rush hours with middle and low wind speeds. A non-linear relationship is found between average modeled concentrations and wind speed with higher concentrations under calm wind speeds. The modeled concentrations are also 20-30% higher in streets that align with the wind direction within $\sim 20^\circ$. We find that streets with higher buildings in the downwind have lower modeled concentrations at the pedestrian level, and similar effects are found for the variability in building heights (including gaps between buildings). The modeled concentrations also decay fast in the first ~ 50 m from the nearest highway and arterial road but change slower further away. This study demonstrates the potential of large eddy simulation in urban air quality modeling, which is a vigorous part of the smart city system and could inform urban planning and air quality management.

1 Introduction

Urban air pollution is one of the greatest threat for human health in the modern world as 55% of the global population are living in cities but more than 80% of them are exposing to air quality levels that exceed the World Health Organization limits (The World Bank, 2020; WHO, 2016). Traffic related emissions are often the major source for urban regions for many air pollutants (e.g. CO, nitrogen oxides, and volatile organic compounds) (Liu and He, 2012). Patterns of traffic-related air pollution in the urban environment has substantial temporal and spatial variability due to unevenly distributed emission sources, complex flow pattern, and physicochemical transformations (Apte et al., 2017). Compounded with the complex and dynamic commuting behavior and crowd dynamics of urban residents, high-resolution air quality information is thus needed for smart-city designers and air pollution mitigation in a “big-data” era (Gao et al., 2019). However, such information is generally not available as accurate ground-based monitoring of air quality at a high spatial resolution is too expensive due to the large number of required instruments even with relatively low-cost sensors (Kumar et al., 2015). The typical monitoring site numbers are ~ 10 even for a megacity with >10 million population and >1000 km² areas, and these sites are often located far away from road networks. For example, there are 9 national air quality stations in Nanjing (<http://hbj.nanjing.gov.cn/>), and 8 air quality monitors in the City of New York

(<https://www.epa.gov/outdoor-air-quality-data/interactive-map-air-quality-monitors>). Alternative approaches such as satellite remote sensing and regional chemical transport models are also spatially coarse (~1-10 km resolution) (van Donkelaar et al., 2010; Zhang et al., 2009). Here we present a very high-resolution air quality model for traffic-related CO air pollution in urban regions using large-eddy simulation.

The impact of traffic emission on urban air quality is associated with a myriad of factors such as emission strength and air pollutant dispersion (Abou-Senna et al., 2013). For example, background meteorological factors such as the wind speed and vertical temperature stratification are known to influence the pollutant dispersion, and the most severe air pollution is associated with calm weather conditions with temperature inversions (Wolf and Esau, 2014). Trees are found to increase turbulence and reduce ambient concentrations associated with traffic emissions at pedestrian height (Jeanjean et al., 2015). While trees are also associated with reduced street ventilation, which leads to higher pollutant concentrations (Vos et al., 2013). The geometry of the street canyon is an important factor: higher buildings and narrower streets cause heavier pollution inside canyon (Fu et al., 2017). The symmetric level of building heights also influence wind and turbulent diffusion and affect pedestrian level concentrations (Fu et al., 2017). Preferable pathways created by the configuration of buildings and streets facilitate longer dispersion of pollutants and influence regions farther away from roads (Wolf et al., 2020).

Numerical models have been applied to model traffic-related air pollution in urban regions. Gaussian plume and puff models have been widely used in such purpose for a long history, e.g. regulatory models such as AERMOD and CALPUFF (US EPA, 2020). These models use statistical method to parameterize turbulent diffusion based on background meteorological conditions and diagnostic building geometry characteristics, and reasonable accurate results can be achieved with representative meteorological input (Rood, 2014). Dispersion models are also nested with regional Eulerian models such as CMAQ and CAMx to bridge the coarse resolution (~km) to street-level (~10 m) (e.g. the ADMS-Urban model (Biggart et al., 2019; Righi et al., 2009)). One drawback of these statistical models is the lack of explicit representation of the air flow and turbulent eddies around landscape and buildings (Sun et al., 2016). The predicting power of these models decreases farther away from sources as they cannot describe the turbulent transport of pollutants by larger eddies which could trap air parcels over longer distances (Wolf et al., 2020). In recent years, computational fluid dynamic models (CFD) that are turbulence-resolving or permitting have been used for urban air quality purpose, starting from ideal conditions (Kurppa et al., 2018; Sanchez et al., 2005; Steffens et al., 2014; Yu and Thé, 2017) to city-wide simulations (Cécé et al., 2016; Jeanjean et al., 2015; Wolf et al., 2020). For instance, Sanchez et al. (2005) simulates reactive pollutants (NO_x, VOC, and O₃) and their reactions in an urban street canyon using the OpenFOAM model. Wolf et al. (2020) utilizes the Parallelized Large-Eddy Simulation Model (PALM) to simulate NO₂ and PM_{2.5} air quality in a coastal city, and successfully identified major sources under high pollution meteorological conditions.

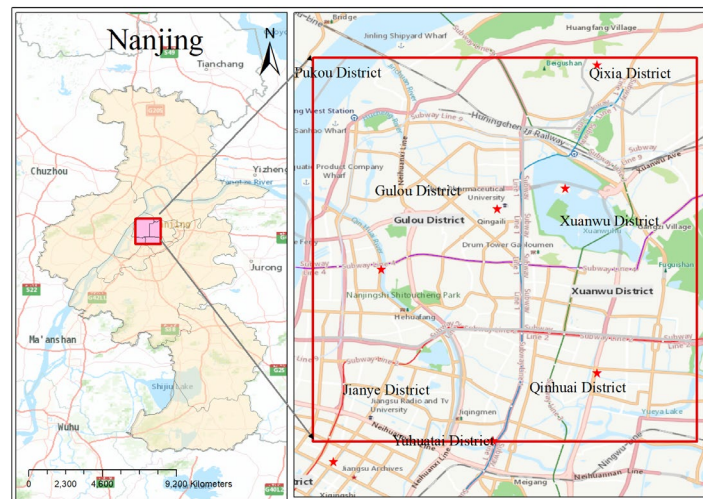
While the high-resolution models map urban air quality at street level, the tremendous high flow of spatial-resolved data are generally lacking proper evaluation against observations. Time series of pollutant concentration data from a limited number of stationary stations are often used to compare to the model results (Biggart et al., 2019; Cécé et al., 2016; Fu et al., 2017). For instance, Biggart et al. (2019) compared their model predictions at street-scale-resolution to eight stations across the city of Beijing with a model domain area of ~400 km². Even though a good correlation is often achieved in these studies, the success in predicting temporal variability does not automatically transfer to spatial variability. In this study, we develop a very high spatial resolution (less than 10 m) model for traffic-related CO air quality based on the PALM model for the city of Nanjing, a megacity in eastern China with more than eight million population. We evaluate the model performance with observations obtained from sensors deployed on taxi platforms, which garner data with comparable spatial resolution to the PALM model. Multiple influencing factors for pedestrian-level air pollution levels are also investigated.

2 Methodology

2.1 PALM Model

We use the PALM model system to simulate the transport of traffic-related emissions in Nanjing. This model is developed by the PALM group at the Leibniz University of Hannover, and has been developed as a turbulence-resolving large-eddy simulation (LES) model system especially for performing on massively parallel computer architectures. We use PALM 4 (version number 3689) for urban applications in this study (The PALM Group, 2020), which includes a dynamic solver for the Navier-Stokes equations and the first

105 law of thermodynamics. The bulk of the turbulent motions in the atmospheric boundary are explicitly resolved (The PALM Group, 2020). To save the model computation time, the pollutants are considered as a passive scalar (i.e. no chemical reactions and deposition), and a neutral stratification condition is assumed (i.e. no buoyancy related terms are calculated). The actual vertical stability varies at Nanjing driven by the nocturnal cycle and large-scale weather patterns but with the neutral condition being the most frequent (Li, 110 2010). A neutral stratification is also considered as the most representative condition because stable and unstable conditions are either unfavorable or favorable for pollutant dispersion (Kurppa et al., 2018). The 5th order upwind scheme of Wicker and Skamarock is used for both momentum and tracer advection (Wicker and Skamarock, 2002). We use CO as a representative pollutant as its relatively long lifetime (months to years) (Jaffe, 1968). So the chemical reactions and dry and wet deposition are generally 115 negligible within the time scale of model simulation (hours). A “Neumann” type boundary condition is applied for CO at the top and bottom of the model domain. A “Cyclic” type is used for its lateral boundary conditions, which yields an infinite and periodically repeating model domain. This is a reasonable assumption as our model domain only covers a portion of the city of Nanjing. For the horizontal wind and pressure, we use a “Dirichlet” type top boundary condition, a “No-slip” condition for the bottom and solid walls, and a “Cyclic” condition for the lateral boundary of the model domain. The flow is assumed to be steady at the inlet. The model explicitly resolves solid obstacles (e.g., buildings) on the Cartesian grid and reduces the 3D obstacle dimension to a 2D topography conforming to the Digital Elevation Model (DEM) format (Letzel et al., 2008). 120



125 Figure 1. Model domain of the PALM model simulation used in the study for the city of Nanjing. The size of the model domain is approximately 10 km × 10 km. Map credit: ESRI 2020.

The model domain covers the core area of Nanjing with the center located at 32.07°N and 118.72°E (Figure 1). The model horizontal resolution is 0.0001°×0.0001° (equivalent to 9.4 m west-east ×11.1 m north-south) with a grid size of 960×960, which covers a total area of about 10 km × 10 km. To represent the CO air 130 quality at pedestrian-level, the model vertical layer depth starts with 2 m from the ground to 12 m height, and stretched by a factor of 1.1 by each layer to a maximum of 40 m depth. The model has a total of 48 vertical layers reaching ~1000 m a.s.l., which is approximately three times higher than the highest building of Nanjing (Zifeng Tower, 340 m height for the top floor). Further increasing the model domain height (e.g., to 2000 m) has no significant impact on the modeled airflow and CO concentrations near the ground as 135 most of the buildings are lower than 150 m (Figure 2A). The model is run for three hours with a time step of 6 seconds. Hourly average data is achieved and we use the results of the last hour for analysis.

The topography of the model consists of two parts: baseline elevation and building heights. The former is based on ASTER global digital elevation model (GDEM) dataset, which has a native resolution of 30 m and is linearly interpolated to the model grid (Computer Network Information Center, 2020). The building 140 data for Nanjing is extracted from Gaode Map (dated as the year 2018, <https://ditu.amap.com>). The building data includes the geographical location of the outer shape of buildings (0.0001°×0.0001° resolution) and their number of floors. We transfer the raw data into the model grid and assume an average floor height of 3 m (Figure 2A). The sum of the elevation and building height data are then used as the

145 topographical data of the PALM model. Due to the large computational cost associated with model simulation, we don't run the model for a consecutive time window with actual meteorological conditions. Instead, we choose a selective combination of meteorological scenarios to represent the variability of meteorological conditions at Nanjing. For each scenario, we assume a constant geostrophic wind field on the top of boundary layer during model simulation. Eight wind directions with 45° apart (N, NE, E, SE, S, SW, W, and NW) are considered. Based on the observed wind speed at the top of local boundary layer
 150 (~500 m) (Chen et al., 2018; He et al., 2018), we choose 10 m/s, 6.5 m/s, and 3 m/s to represent high, median, and weak wind conditions, respectively. This results in a total of 48 scenarios, which is limited by our computational capacity. We thus consider our study as a demonstration of the model approach and it can be improved by more scenarios.

2.2 Traffic Emissions

155 We use a “standard road length” approach to assign the total traffic emissions to individual road based on different road types and traffic flows (Zheng et al., 2009). We first transfer the actual road length (L) into total standard road length (TSL , km) of Nanjing using road conversion coefficient (W):

$$TSL = \sum_{j=1}^o \sum_{i=1}^m \sum_{k=1}^n L_{i,j,k} \times W_{i,j,k} \quad (1)$$

160 where i , j , and k represent the area types (i.e., urban and suburban areas), grid cell index, and road type, respectively, with m , n , and o representing the total numbers of area types, grid cells, and road types, respectively, and the W is calculated as:

$$W_{i,j,k} = \frac{TF_{i,j,k}}{STF} \quad (2)$$

where $TF_{i,j,k}$ is the traffic flow for the k th road type and i th area type in grid j (in standard vehicles) and STF is the standard traffic flow (in standard vehicles).

165 The traffic emission (GE_j) of each grid cell j is calculated based on total standard road length in the grid cell (GSL_j) and the standard emission intensity per standard unit length (SEI , t/km):

$$GE_j = GSL_j \times SEI \quad (3)$$

where SEI is calculated based on the TSL calculated in equation (1) and the city-level-based vehicle emission inventories (E , t):

170
$$SEI = \frac{E}{TSL} \quad (4)$$

and GSL_j is calculated as:

$$GSL_j = \sum_{i=1}^m \sum_{k=1}^n L_{i,j,k} \times W_{i,j,k} \quad (5)$$

We also assign the daily mean GE_j to each hour based on the diurnal variation of the 24-hour traffic flow (Figure 2B). The diurnal variation of the traffic flows and subsequently the traffic emissions at Nanjing are based on the Gaode Map (<https://report.amap.com/detail.do?city=320100>). The total traffic CO emissions in the model domain are 0.77 and 0.60 kg s⁻¹ for rush and non-rush hours, respectively.

175

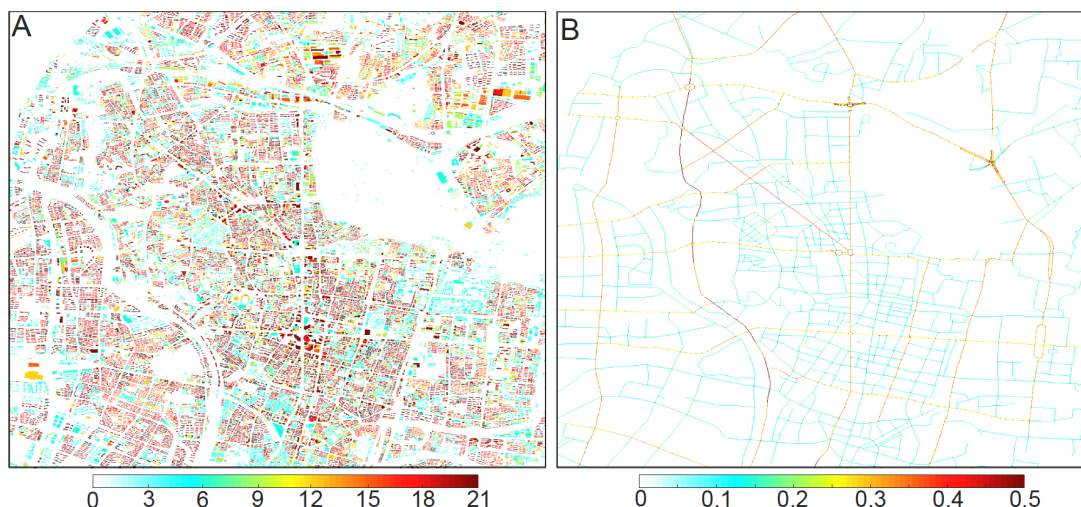


Figure 2. Spatial distribution of (A) building heights (m) and (B) traffic CO emissions ($\text{mg cell}^{-1} \text{s}^{-1}$) (during rush hours) in the model domain.

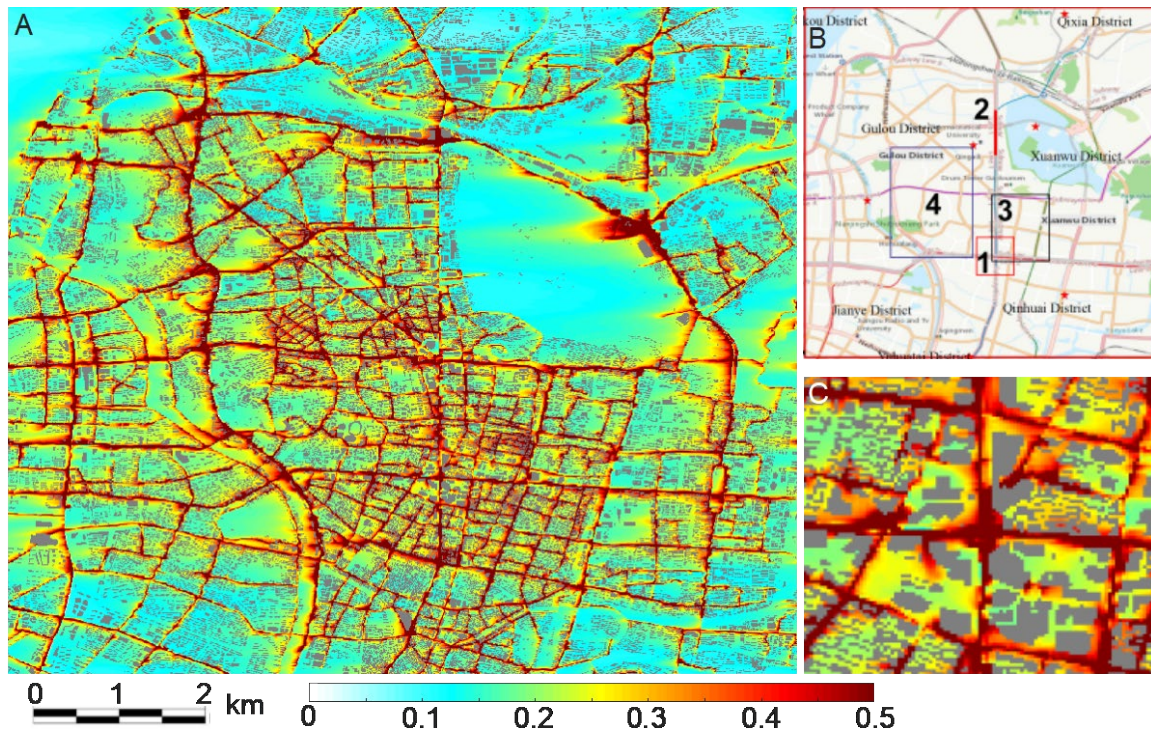
180 2.3 Taxi Sensor Data

We evaluate the model results with observations collected from a mobile platform that is performed during September 2019 - October 2020. The details of the platform instrument and its deployment are described with detail in the companion paper of this study (Wang et al., 2020). Briefly, we use two XHAQSN-508 instrument (dimensions: $290 \times 81 \times 55$ mm; weight: 1.0 kg) produced by Hebei Sailhero Environmental Protection High-tech Co., Ltd. (Hebei, China), which includes an internal CO gas sensor (detectable CO range: 0 to 50 mg m^{-3}) and is installed on the top of two Nanjing taxis (~ 1.5 m above ground). The sensor is capable of continuous measuring CO concentrations at a programmable frequency of once per 10 s. The inlet system is also optimized to minimize self-sampling and gas sampling losses. The spatial coordinates are also recorded by a GPS device included in this instrument (U-blox, Switzerland). The monitoring and location data are simultaneously transmitted to a remote server in real time through wireless communication, and the real time measurement data can be viewed through a web page or an Android app. One major advantage of this mobile platform is the minimum maintenance cost, as samples are automatically collected during the operation of the taxis. An analyze of the sensing power, defined as the fraction of city road network sampled by a taxi fleet, also demonstrates that a remarkably small number of taxis can scan a large number of streets (O’Keeffe et al., 2019; Wang et al., 2020).

The instrument is calibrated once per month against a stationary instrument (T300 CO Analyzer by Teledyne API) at the SORPES observation station in the Xianlin Campus of Nanjing University (https://as.nju.edu.cn/as_en/obsplatform/list.htm). During calibration, the instrument is taken back to the campus and placed back-to-back to the calibrating instrument in the station. The calibration lasts for at least seven days, and the parameters for the sensor retrieving algorithm are adjusted to make sure the differences between the sensor retrieved data and the station data is $< 1\%$ (Wang et al., 2020). As only traffic-related emissions are considered in the PALM model, we add the model results to the background concentrations of Nanjing for comparing to the observed data by the mobile platform (but the pure model output is used for other analysis). The hourly background CO concentrations are calculated as the minimum of measurements from all the nine national air quality monitoring stations in Nanjing metropolitan area (<http://beijingair.sinaapp.com/>). Seven of these stations are located inside the model domain representing different functioning districts of the city. The remaining two are located at the suburbs to the west and northeast of the city center, which could be a reasonable representative for background concentrations depending on wind directions. Corresponding hourly meteorological data of Nanjing city is obtained from the National Meteorological Information Center of China (<http://data.cma.cn/en>). We include data on both rainy and non-rainy days as CO is not dissolvable.

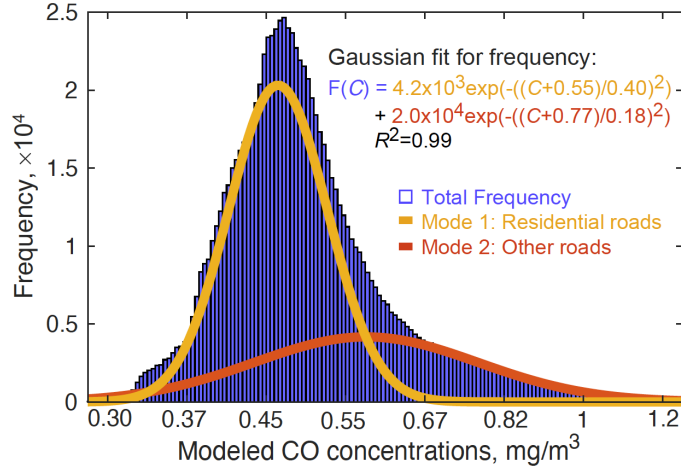
3 Results and Discussion

3.1 Very High-Resolution Modeled CO Concentration



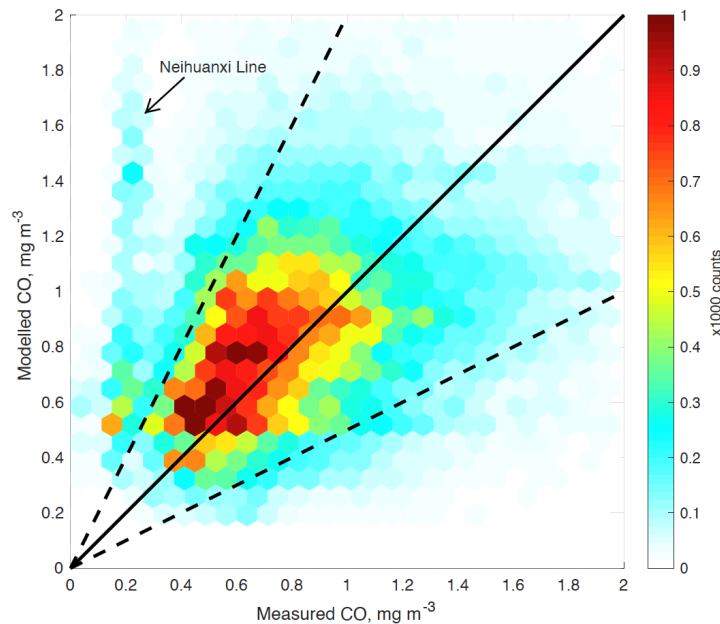
215 Figure 3. Modeled ground-level CO concentrations (mg/m^3) during rush hours by the PALM model with
 wind from the east and speed as 6.5 m/s in the top of the boundary layer (A). Panel B shows the
 220 corresponding city map. Panel C shows a zoom in over Xinjiekou area with boundary shown as a red
 rectangle in panel B (Rectangle 1). Grey areas represent top of buildings. Map credit: ESRI 2020.

220 Figure 3 shows an example of the spatial distribution of the modeled traffic-related ground-level (0-2 m
 above ground) CO concentrations during peak hours (with an east wind and 6.5 m/s at the top of boundary
 layer). The very high resolution of the model reveals a detailed geographical dispersion pattern of CO
 concentrations in and out of the road network. The average modeled CO concentrations inside the road
 network are $0.76 \text{ mg}/\text{m}^3$ (with 25% and 75% percentiles as $0.45 - 0.94 \text{ mg}/\text{m}^3$, respectively), which are
 225 much larger than those outside the network: $0.22 (0.14 - 0.24) \text{ mg}/\text{m}^3$. The lowest concentrations are
 modeled over regions with less dense road network and water bodies ($\sim 0.1 \text{ mg}/\text{m}^3$). Higher ground-level
 concentrations are modeled over major highways with substantially higher emissions than other roads
 (Figure 2B). The concentrations are also higher over interceptions of roads as the emissions are specified as
 the sum of that of the intercepted roads. The model simulates clear plumes downwind of major roads,
 especially if no obstacles existed in that direction. The most apparent plume is simulated in the northeast of
 230 the Xuanwu Lake (refer to the map in Figure 3B). The high emissions are swept for about 1 km westward
 from a traffic center at the northeast edge of the lake. Highways such as the Neihuanxi Line also produce
 apparent westward plumes, whereas downwind buildings may cause extra turbulence to smoothen out the
 signal. By contrast, the emissions from regions with dense buildings are generally trapped within the street
 canyons (e.g. the city center), with leakage from gaps between buildings (Figure 3C). Overall, the modeled
 235 ground-level concentrations follow a two-mode Gaussian distribution (i.e. a sum of two Gaussian functions,
 Figure 4), with one for residential streets (with a geometric mean of $0.17 \text{ mg}/\text{m}^3$) and the other for arterial
 roads, highways, and the nearby regions (with a geometric mean of $0.28 \text{ mg}/\text{m}^3$).



240 Figure 4. Frequency distribution of modeled ground-level CO concentrations during rush hours under east wind and 6.5 m/s at the top of boundary layer. The distribution is fitted with a two-mode Gaussian model. The yellow (residential streets) and orange (arterial roads, highways, and the nearby regions) curves represent the two Gaussian modes.

3.2 Model Evaluation



245 Figure 5. Comparison of measured and modeled ground-level CO concentrations. Colors represent the total number of matching measured and modelled values contained within distinct hexagons. Black line indicates 1:1 and dashed lines mark a factor of 2 difference.

The rich information provided by the model is compared to observations obtained by the mobile monitoring platform (Figure 5 and 6). We sample the hourly-mean model results with the same location, emission level (rush or non-rush hours), and wind speed/directions as the observations. We aggregate the model results into a 100 m resolution due to the relatively low sampling frequency of the mobile sampler (10 s, equivalent to ~100 m), which is indeed a drawback and can be improved by higher time-frequency sensors. The sum ($0.92 \pm 0.40 \text{ mg/m}^3$) of model results that are caused by traffic-related sources ($0.36 \pm 0.32 \text{ mg/m}^3$) and regional background concentrations ($0.56 \pm 0.28 \text{ mg/m}^3$) agree well with the measured CO concentrations ($0.90 \pm 0.58 \text{ mg/m}^3$, $n = 114,502$) ($p < 0.01$). Point-by-point comparison reveals that most of the data points fall near the 1:1 line and are within lines for a factor of 2 difference (Figure 5). The model tends to overestimate the measured CO concentrations over the Neihuanxi Line (the line of points on the left of Figure 5, location marked in Figure 1), which is a viaduct with better ventilation than ground-level

roads. However, our model considers all the emissions at the ground-level thus simulates much higher concentrations than observations over this line. This also demonstrates the significant air quality benefit of building viaduct in an urban environment.

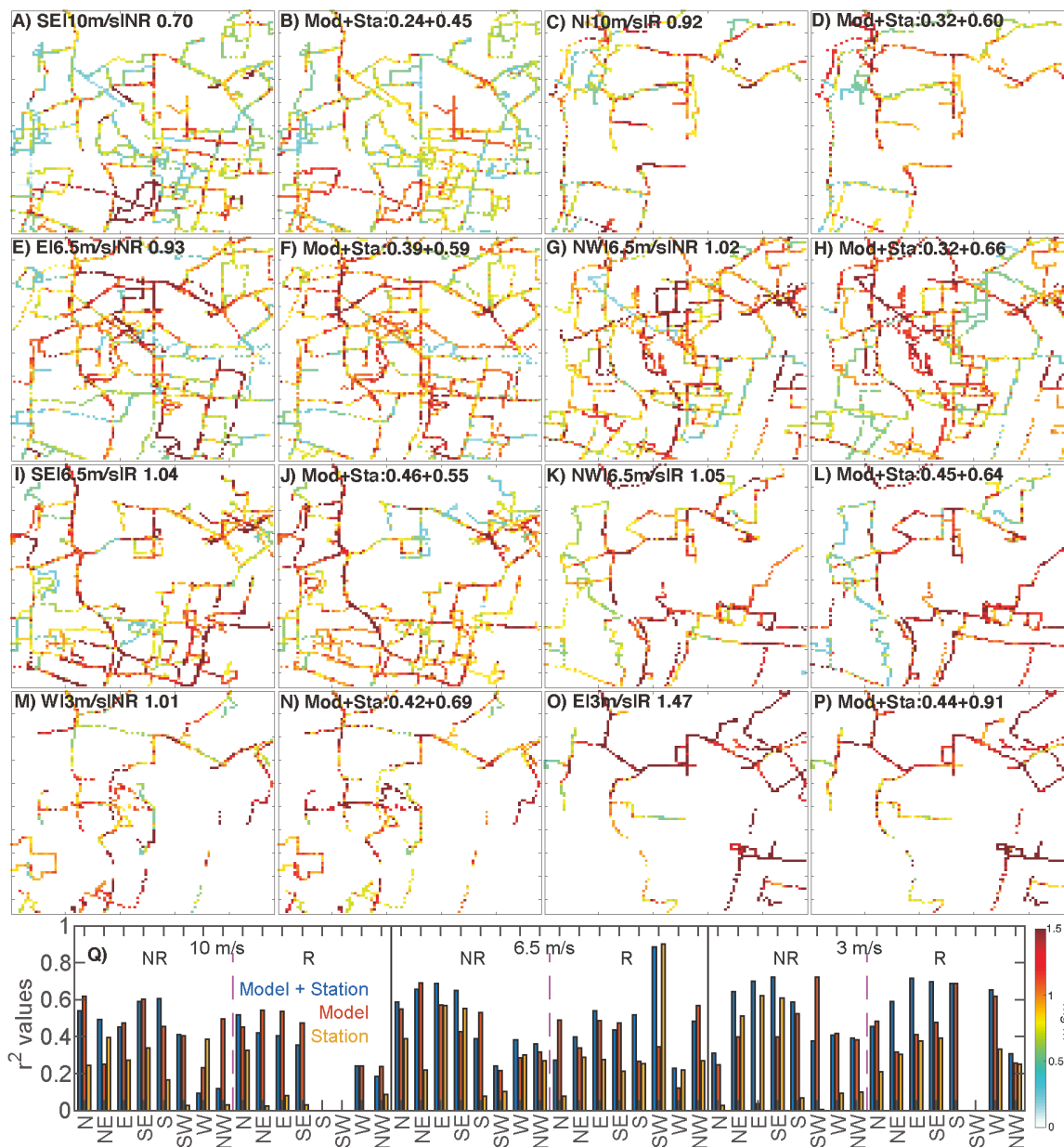
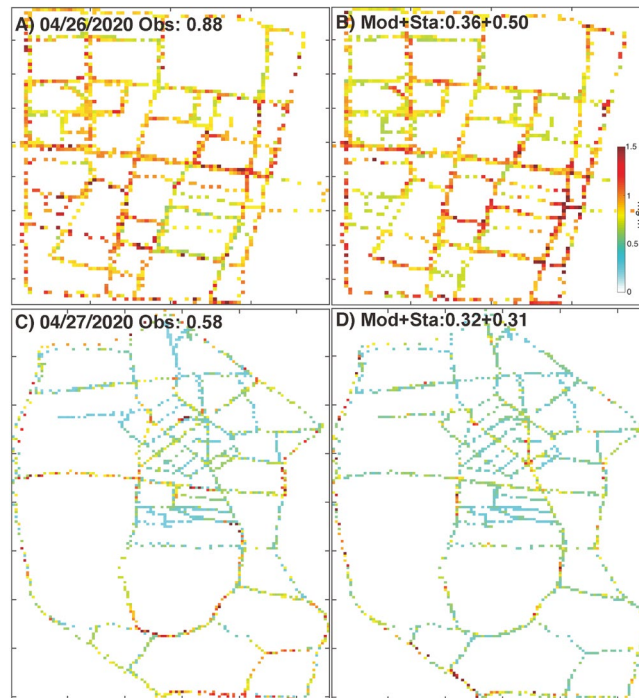


Figure 6. Comparison between taxi sensor measured (odd columns) and modeled (even columns) ground-level CO concentrations for selected combinations of wind speed, directions, and rush/non-rush hours. As the taxi sensor data has a temporal resolution of 10 s (roughly equivalent to 100 m given an average vehicle speed of 40 km/h), both the measurements and model results are regridded to a 100 m resolution grid. The wind and emission information is shown on top of panels in this format: “wind direction | wind speed | emission level rush or non-rush hours”. The mean of the data is shown on top of each panel, with the modeled one as the sum of the model output and regional background from national stations. Panel Q shows the coefficients of determination (r^2) of a linear regression between taxis sensor data and model/station data under different emission and meteorological conditions. Blue bars represent the regression between measured and model + regional background, while red and yellow bars are for the measured vs model only and measured vs station data only, respectively. Note the color bar for panel A-P is in panel Q.

275 As both the modeled and measured CO concentrations vary drastically, we group the data based on the
 sampling time and meteorological conditions and compare the spatial patterns of model results and the
 measurements in Figure 6. We find the model captures many of the observed spatial features under a
 variety of emission and meteorological conditions. Take 10 m/s east wind during non-rush hours as an
 280 example (Figure 6A and 6B), higher concentrations are modeled and measured in the city center, the
 highway in north city, and the arterial roads in the southwest corner of the model domain, while lower
 concentrations are in the middle of the west part and southeast corner of the model domain. Similar levels
 of agreement between the spatial patterns of measurements and model results are achieved for other
 conditions.



285 Figure 7. Comparison between taxi sensor measured (A and C) and modeled (B and D) ground-level CO
 concentrations during two intensified observation campaigns during April 26-27, 2020. The locations of the
 campaigns are shown in Figure 3B (Rectangle 3 and 4 for the 26th and 27th, respectively).

Figure 6Q shows that the coefficients of determination (r^2) are generally higher (0.51 ± 0.16) during non-
 rush hours with middle and low wind speeds, due to the relatively larger sample sizes under such conditions.
 290 The r^2 values for high wind condition and rush hours will be increased as the accumulation of taxi sensor
 data (either longer sampling period or more sensors). As the model data used in this comparison includes
 the regional background, we calculate the r^2 values if only using the station data to rule out the possibility
 that the agreement in spatial pattern is caused by station data. Also taking the r^2 values during non-rush
 hours with middle and low wind conditions as an example, only using station data lower the r^2 values to
 295 0.28 ± 0.23 . This indicates that our model indeed carries useful spatial information that significantly
 improve the comparison with sensor data.

One drawback of the taxi platform is that the popular streets are easily covered and sampled repeatedly, but
 unpopular segments are rarely visited (O’Keeffe et al., 2019; Wang et al., 2020). The sensor data used in
 this study mainly cover the highway and arterial roads, but generally leave the model results for residential
 300 streets unevaluated. We therefore supplement the routine taxi operation data with two one-day taxi cruise
 campaigns, which cover all the public roads in two representative regions (especially including the
 residential ones less visited by taxis), as shown in Figure 7 (the location of campaign is shown in Figure
 3B). Overall, the model captures the observed spatial patterns reasonably well with r^2 values for the two
 campaigns as 0.50 and 0.37, comparable to the data collected during normal taxi operations (Figure 6Q).
 305 The first campaign is in the city center (Figure 7A and 7B) with the traffic-related CO concentrations
 relatively more uniformly compared to the second one, which covers a larger area and includes highways,
 arterial, and residential roads (Figure 7C and 7D). The model also captures the relatively higher

concentrations in the highway near the west edge in the second campaign (Figure 7C and 7D), as well as the generally decreasing concentrations from highways, arterial roads, to residential ones. Even though the model has highly simplified setting-ups and the mobile sensors have relatively large uncertainties compared with reference method (Wang et al., 2020), the agreement between them lend both approaches confidence.

3.3 Influencing Factors

3.3.1 Emissions, wind speed and directions

Figure 8 shows the mean ground level CO concentrations over the whole model domain under different emission strengths and meteorological factors. We find the wind speed is an important controlling factor for modeled CO concentrations. The average ground-level CO concentrations during rush hours with a wind speed of 3 m/s range 0.37-0.46 mg/m³. The concentrations with 3 m/s wind are ~2.4 and ~1.8 times higher than those with 10 m/s (0.16 – 0.19 mg/m³) and 6.5 m/s (0.21 – 0.25 mg/m³) wind speeds, respectively. The concentration differences between 10 m/s and 6.5 m/s are about 30%. It clearly suggests a non-linear dependence of concentrations on wind speed with much higher concentrations over stagnant conditions, consistent with previous studies (Mumovic et al., 2006; Wolf et al., 2020). Indeed, convective transport of pollutant is greatly reduced under low wind speed conditions, which elevates CO concentrations at the pedestrian level. On the other hand, the response to emission strength is almost linear with concentrations during rush hours are 27% higher than non-rush hours given the same meteorological conditions. The concentrations with different wind directions range ~20%, with consistent highest concentration for west wind and lowest for northeast wind. This pattern could be explained by the spatial pattern of emission distributions: with higher emissions in the west part of the model domain and lower over the northeast (where a big lake locates). Wind from cleaner regions (e.g. northeast) helps to blow out the traffic-related emission located at the other side of the model domain, and vice versa.

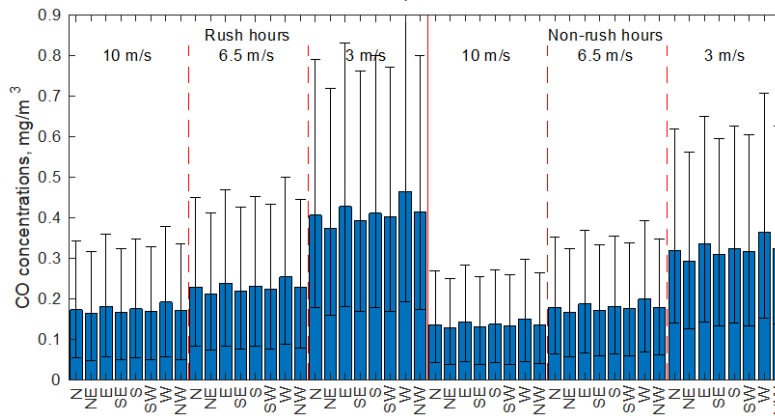
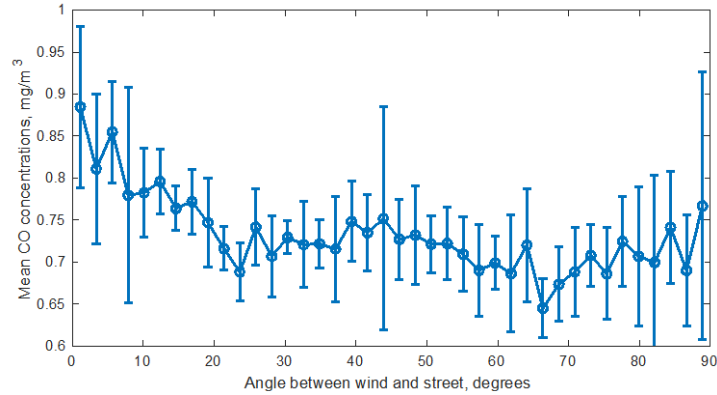


Figure 8. Mean modeled ground-level CO concentrations (with 30% and 70% percentiles) over the whole model domain with different wind speed, directions, and emission levels.

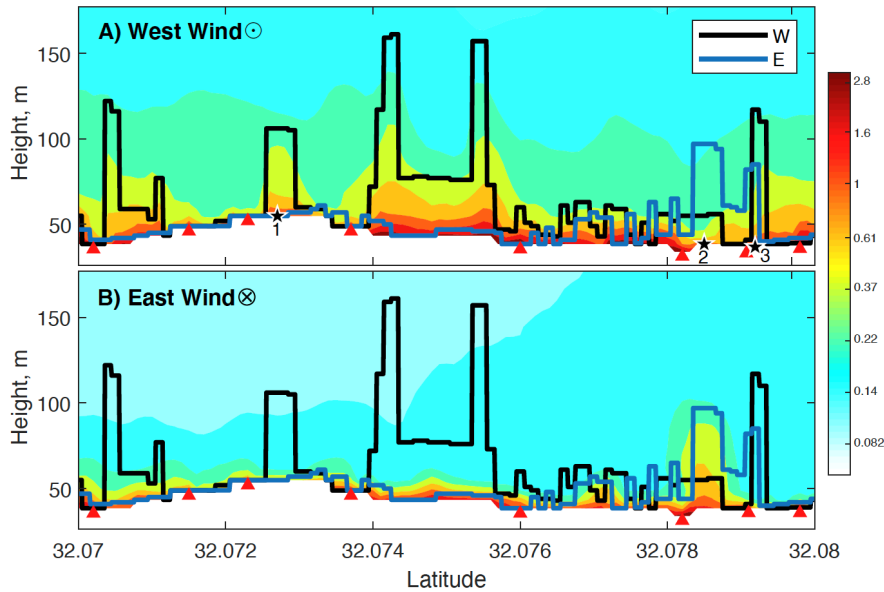
3.3.2 Street direction

Even though the wind direction seems not to be an important influencing factor for model domain-average concentrations, it is a vital factor for individual street canyons. Figure 9 shows the relationship between the mean ground-level CO concentrations and the angle between wind and street directions. We find the modeled concentrations are the highest when the wind direction aligns with streets. The concentrations decrease until the angle increases to ~20° but no significant differences are modeled when the angles continue to increase. A wind direction parallel with the street mainly transports CO along the canyon, which traps pollutant inside of the street. By contrast, a perpendicular wind can blow pollutant outside of the canyon through gaps between buildings, which reduces the CO concentrations inside. Similar results have been found in smaller scale studies. For example, through comparing pollutant levels with different wind directions, Kurppa et al. (2019) found lower pedestrian-level pollution when wind direction is closer to perpendicular with a boulevard and suggested the shortest wall parallel to the road to increase ventilation and create optimal air quality. Solazzo et al. (2011) found both the highest observed and modeled NOx concentrations inside a street canyon under a “quasi-parallel” situation. Mumovic et al. (2006) also suggested an accumulation effects along those canyons whose axes are parallel to the wind direction.



350 Figure 9. Influence of the angle between the directions of the wind and the street on modeled ground-level CO concentrations. Wind speed is specified as 6.5 m/s with emissions as that during rush hours.

3.3.3 Building heights



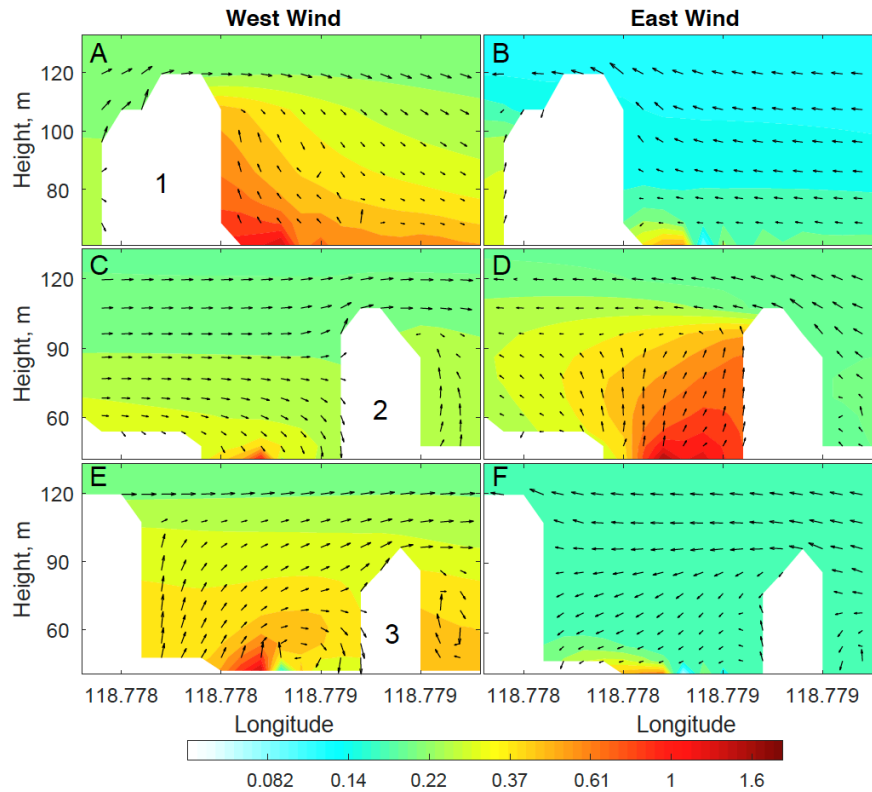
355 Figure 10. Spatial distribution of modeled CO concentrations under west (A) and east (B) wind directions (3 m/s) in latitude-height cross sections along Zhongyang Road during rush hours (marked as red line 2 in Figure 3B). The outlines of buildings on both sides of the road are shown as black (west side) and blue (east side) lines. Red triangles show the locations of major road intersections.

360 The influence of street and wind directions on modeled CO concentrations is more obvious in a latitude-height cross section along a north-south direction street (Figure 10). Figure 11 shows the CO concentrations in three longitude-height cross sections (marked as 1, 2, and 3 in Figure 10A) to illustrate the leakage plumes from gaps between buildings. The modeled CO concentrations decrease sharply with height, as the sources are from near the ground (Fu et al., 2017). The buildings in the east side of this road that is close to the lake are lower than those in the west. The modeled CO concentrations are extended to a higher altitude behind the tall buildings under west wind conditions (Figure 10A). The upwind buildings cause wake flows that transport pollutant toward the buildings at pedestrian level and make an accumulation zone at the leeward corners (Figure 11A and 11D). By contrast, the traffic-related emissions are not elevated to a higher altitude with east wind due to the short buildings on that side (Figure 10B). Buildings located at downwind of emission sources tend to create a flow pattern that blows pollutant away from them near the ground (Figure 11B and 11C). Previous studies also found similar concentration gradients between leeward and windward of buildings when wind direction is perpendicular to the street canyon (Fu et al., 2017; Mumovic et al., 2006; Solazzo et al., 2011). For example, Fu et al.(2017) found that pollutants emitted inside the street canyon with lower building heights in leeward than windward tend to disperse out of the

365

370

canyon, and vice versa. When buildings exist both sides of the street, the flow and concentration distributions are largely determined by which side the taller building locates (Figure 11E and 11F). The concentrations inside the street canyon are higher if the upwind building is taller than the downwind one.



375

Figure 11. Spatial distribution of modeled CO concentrations and wind vectors in longitude-height cross sections along three buildings in Zhongyang Road (marked as stars in Figure 10A). The concentrations distributions under west (A, C, and E) and east (B, D, and F) winds are shown. Note the vertical velocity is scaled by a factor of 2.5.

380

We also evaluate the relationship between the mean ground-level CO concentrations and the building heights in the upwind and downwind side of the street canyon in the whole model domain (Figure 12). We find the existence of upwind buildings generally increases the CO concentrations inside the street canyon compared to cases without buildings in that direction (i.e. zero building height) (Figure 12A). As discussed above, this is associated with the wake flow pattern of the building (Figure 11A, 11D and 11E). The concentrations show no significant difference when the upwind building are ~10-45 m height, but decrease when building height further increases (Figure 12A). The influence of downwind building heights are largely monotonically with lower concentrations for higher heights. The interaction of upwind and downwind building heights is evaluated by their differences (e.g. upwind - downwind heights). Overall, the concentrations are higher over streets canyons with higher upwind buildings, but the enhancement in concentrations begin to decrease if the difference is larger than ~30 m, consistent with Figure 12A. Similarly, higher downwind buildings bring down the concentrations inside the canyon monotonically, consistent with Figure 12B.

385

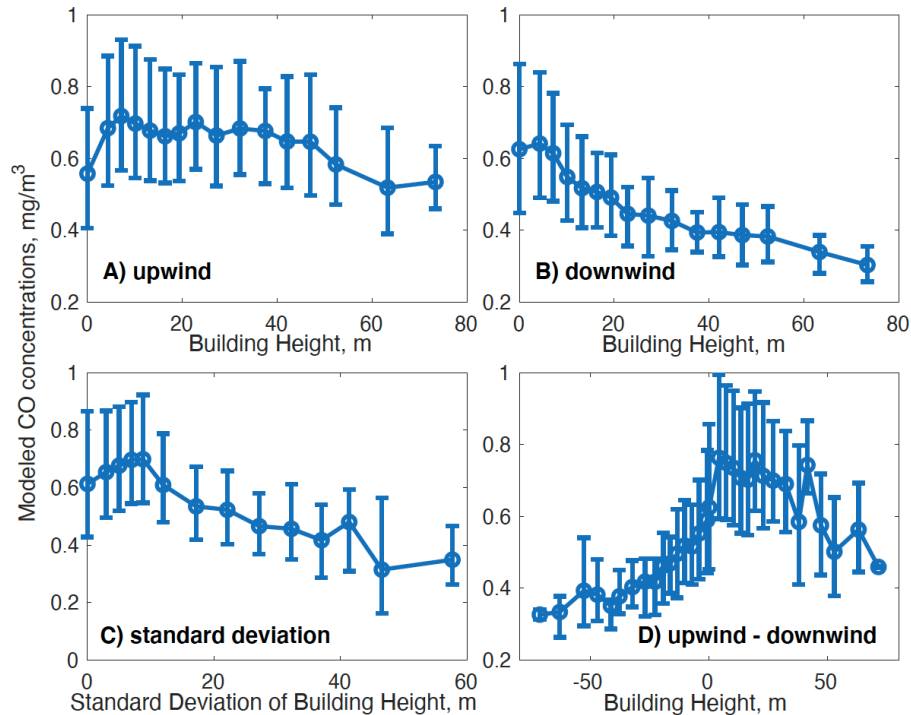
390

395

Figure 12C illustrates the influence of the variation of building heights within 50 m distance on the modeled ground-level CO concentrations. It indicates that the concentrations first increase when the standard deviation of building heights increase from 0 to ~10 m, reflecting the trapping effect of upwind buildings compared to flat surfaces. The concentrations significantly decrease when the nearby buildings are more variable. The variation in building heights has been demonstrated to increase the ventilation rates and the vertical turbulent flux density, which helps to lower pedestrian-level pollution (Kurppa et al., 2018). Fu et al. (2017) also found the concentration inside the street canyon first increase with the symmetric index of building heights, but decreases when the index becomes larger. These results suggest putting

400

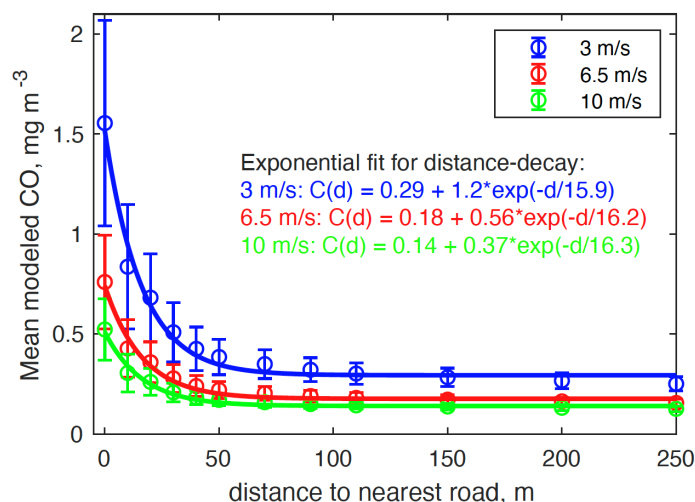
higher building in the prevailing downwind side of a road with large variability in building heights and multiple gaps between them generate the best pedestrian-level air quality.



405 Figure 12. Relationship between geometric mean modeled ground-level CO concentrations and building heights in the upwind (A), downwind (B) directions, (C) the standard deviations of nearby (within 50 m distance) building heights, and (D) the difference between the upwind and downwind building heights. Wind speed is assumed to be 6.5 m/s and emissions are specified as that during rush hours.

3.3.4 Distance to major roads

410 As discussed above, the modeled ground-level CO concentrations are higher inside the road network than outside of it. Figure 3 shows a clear decreasing trend of modeled concentrations from the road network to residential regions far away from the major roads. We thus calculate the distance from a given location to the nearest major roads (d), which include highways and arterial roads with emissions considered in this study (Figure 2B). Figure 13 shows the mean modeled ground-level CO concentrations (C) and their standard deviations as a function of d . We used an exponential equation to fit this function: $C(d) = \alpha + \beta \exp(-d/k)$ following Apte et al. (2017), where α represents the modeled background contribution from traffic-related sources, i.e. $C(\infty)$, β is the sensitivity of C to d , and k represents the spatial scale of the decay of C. The equation fits the modeled means well, despite the relatively large standard deviations especially when d is less than ~ 50 m (Figure 13). We find the α value decreases as wind speed increases, indicating lower background values with higher wind speed as discussed in the section 3.3.1. Similarly, the β values
 420 also decrease with higher winds. However, we find nearly identical k values for all the wind speeds, suggesting that it is a universal parameter controlled by the atmospheric lifetime of pollutants but not influenced by meteorological conditions. Indeed, Apte et al. (2017) also found different k values for NO, BC, and NO₂. Our k values are much smaller than those calculated by Apte et al. (2017) because they only consider the distance to the nearest highways and their d values are much larger than ours. Our calculates
 425 are close to the model results of Biggart et al. (2019) that NO₂ concentrations also become quasi-stable ~ 50 m away from a major highway.



430 Figure 13. Relationship between the modeled ground-level CO concentrations and the distance to the nearest major roads (assuming east wind with emissions during rush hours). The circles and error bars are means and standard deviations, respectively.

4 Conclusions and Implications

435 This study demonstrates the potential of large eddy simulation in urban air quality modeling. Future directions of the model include a more dynamic emission inventory that considers real-time vehicle speed and traffic congestion (Pan et al., 2016). The model frame is also readily expandable to include other pollutant sources (e.g. point and area sources), multiple pollutants, and their chemical reactions (Wolf et al., 2020; Zhong et al., 2015). More realistic meteorological conditions possibly nudging from larger-scale weather and climate data could replace the limited number of assumed scenarios as adopted in this study (Heinze et al., 2016).

440 The revealed high-resolution spatial variability and its association with underlying meteorological conditions are useful for developing parameterization schemes for statistical models like AERMOD and ADMS-Urban, and land use regression models (Jerrett et al., 2005). As high-resolution information on urban building and traffic distribution is becoming more available, the approach could be relatively easily applied to other cities. The simulated tremendously high-resolution maps of concentrations in all major urban areas will be a vigorous part of smart city system (Silva et al., 2018), and serve as a data assimilation platform for many other products from satellite remote sensing and mobile platforms. The model results give hints for source contribution and hot-spot for urban air pollution, which could inform urban planning, air quality management, and risk mitigation. Combined with personal GPS data, the revealed very high-resolution of air quality map can inform epidemiological studies, health risk analysis, and alter personal behavior (Gao et al., 2019; Larkin and Hystad, 2017).

Code/Data availability

The model code and validation data used in this work are available on the EBMG homepage: <https://www.ebmg.online>.

455 Author contribution

YZ and NZ designed the research; YZ, XY, SW, and ZW performed model simulations; YZ, LD, SW, YM, MY, YL, and QL analyzed data; XH and HW provided emission data; SW, LW, XC, AD, LZ, and YX provided validation data; YZ, SW, LD, and HW wrote the paper.

460 Competing interests

The authors declare that they have no conflict of interest.

Acknowledgments

465 This study was supported by the National Key R&D Program of China (2019YFA0606803), National Natural Science Foundation of China (71974092), Start-up fund of the Thousand Youth Talents Plan,

Jiangsu Innovative and Entrepreneurial Talents Plan, and the Collaborative Innovation Center of Climate Change, Jiangsu Province. We are grateful to the High Performance Computing Center (HPCC) of Nanjing University for doing the numerical calculations in this paper on its blade cluster system. We thank Rong Ye and Liang Luo for sample collection.

470

References

- Abou-Senna, H., Radwan, E., Westerlund, K. and Cooper, C. D.: Using a traffic simulation model (VISSIM) with an emissions model (MOVES) to predict emissions from vehicles on a limited-access highway, *J. Air Waste Manag. Assoc.*, 63(7), 819–831, doi:10.1080/10962247.2013.795918, 2013.
- 475 Apte, J. S., Messier, K. P., Gani, S., Brauer, M., Kirchstetter, T. W., Lunden, M. M., Marshall, J. D., Portier, C. J., Vermeulen, R. C. H. and Hamburg, S. P.: High-Resolution Air Pollution Mapping with Google Street View Cars: Exploiting Big Data, *Environ. Sci. Technol.*, 51(12), 6999–7008, doi:10.1021/acs.est.7b00891, 2017.
- Biggart, M., Stocker, J., Doherty, R. M., Wild, O., Hollaway, M., Carruthers, D., Li, J., Zhang, Q., Wu, R., 480 Kotthaus, S., Grimmond, S., Squires, F. A., Lee, J. and Shi, Z.: Street-scale air quality modelling for Beijing during a winter 2016 measurement campaign, *Atmos. Chem. Phys. Discuss.*, (2), 1–35, doi:10.5194/acp-2019-783, 2019.
- Bureau Statistics of Nanjing Municipal: Nanjing Statistical Yearbook, 2020.
- Cécé, R., Bernard, D., Brioude, J. and Zahibo, N.: Microscale anthropogenic pollution modelling in a small 485 tropical island during weak trade winds: Lagrangian particle dispersion simulations using real nested LES meteorological fields, *Atmos. Environ.*, 139, 98–112, doi:10.1016/j.atmosenv.2016.05.028, 2016.
- Chen, C., Meng, D. and Sun, P.: Research on Change Characteristics of wind speed at mid-low altitude layer over China based on radiosonde wind speed data, *J. Arid Meteorol.*, 36(1), 82–89, 2018.
- Computer Network Information Center: Geospatial Data Cloud, [online] Available from: 490 https://www.gscloud.cn/sources/dataset_desc/421?cdataid=302&pdataid=10&datatype=gdem_utm2, 2020.
- van Donkelaar, A., Martin, R. V., Brauer, M., Kahn, R., Levy, R., Verduzco, C. and Villeneuve, P. J.: Global estimates of ambient fine particulate matter concentrations from satellite-based aerosol optical depth: Development and application, *Environ. Health Perspect.*, 118(6), 847–855, doi:10.1289/ehp.0901623, 2010.
- 495 Fu, X., Liu, J., Ban-Weiss, G. A., Zhang, J., Huang, X., Ouyang, B., Popoola, O. and Tao, S.: Effects of canyon geometry on the distribution of traffic-related air pollution in a large urban area: Implications of a multi-canyon air pollution dispersion model, *Atmos. Environ.*, 165, 111–121, doi:10.1016/j.atmosenv.2017.06.031, 2017.
- Gao, Q. L., Li, Q. Q., Zhuang, Y., Yue, Y., Liu, Z. Z., Li, S. Q. and Sui, D.: Urban commuting dynamics in response to public transit upgrades: A big data approach, *PLoS One*, 14(10), 1–18, 500 doi:10.1371/journal.pone.0223650, 2019.
- He, J., LU, C., XIE, S., Jiang, Y. and Han, Z.: Assessing the performance of wind profile radar in Nanjing and its application, *J. Meteorol. Sci.*, 38(3), 406–415, 2018.
- Heinze, R., Moseley, C., Böske, L. N., Muppa, S., Maurer, V., Raasch, S. and Stevens, B.: Evaluation of large-eddy simulations forced with mesoscale model output for a multi-week period during a measurement 505 campaign, *Atmos. Chem. Phys. Discuss.*, 1–37, doi:10.5194/acp-2016-498, 2016.
- Jaffe, L. S.: Ambient carbon monoxide and its fate in the atmosphere, *J. Air Pollut. Control Assoc.*, 18(8), 534–540, doi:10.1080/00022470.1968.10469168, 1968.
- Jeanjean, A. P. R., Hinchliffe, G., McMullan, W. A., Monks, P. S. and Leigh, R. J.: A CFD study on the effectiveness of trees to disperse road traffic emissions at a city scale, *Atmos. Environ.*, 120, 1–14, 510 doi:10.1016/j.atmosenv.2015.08.003, 2015.
- Jerrett, M., Arain, A., Kanaroglou, P., Beckerman, B., Potoglou, D., Sahsuaroglu, T., Morrison, J. and Giovis, C.: A review and evaluation of intraurban air pollution exposure models, *J. Expo. Anal. Environ. Epidemiol.*, 15(2), 185–204, doi:10.1038/sj.jea.7500388, 2005.
- 515 Kumar, P., Morawska, L., Martani, C., Biskos, G., Neophytou, M., Di, S., Bell, M., Norford, L. and Britter, R.: The rise of low-cost sensing for managing air pollution in cities, *Environ. Int.*, 75, 199–205, doi:10.1016/j.envint.2014.11.019, 2015.
- Kurppa, M., Hellsten, A., Auvinen, M., Raasch, S., Vesala, T. and Järvi, L.: Ventilation and air quality in city blocks using large-eddy simulation-urban planning perspective, *Atmosphere (Basel)*, 9(2), 1–27, doi:10.3390/atmos9020065, 2018.
- 520 Kurppa, M., Karttunen, S., Hellsten, A. and Järvi, L.: High-resolution urban air quality modelling using PALM 6.0, , 16(1), 2019, 2019.

- Larkin, A. and Hystad, P.: Towards Personal Exposures: How Technology Is Changing Air Pollution and Health Research, *Curr. Environ. Heal. reports*, doi:10.1007/s40572-017-0163-y, 2017.
- Letzel, M. O., Krane, M. and Raasch, S.: High resolution urban large-eddy simulation studies from street canyon to neighbourhood scale, *Atmos. Environ.*, 42(38), 8770–8784, doi:10.1016/j.atmosenv.2008.08.001, 2008.
- Li, C.: Features of the atmospheric stability at Nanjing area, in *Proceedings of the 9th forum of meteorological sciences at Yangtze River Delta*, pp. 1–7., 2010.
- Liu, H. and He, K.: Traffic optimization: A new way for air pollution control in China’s urban areas, *Environ. Sci. Technol.*, 46(11), 5660–5661, doi:10.1021/es301778b, 2012.
- Mumovic, D., Crowther, J. M. and Stevanovic, Z.: Integrated air quality modelling for a designated air quality management area in Glasgow, *Build. Environ.*, 41(12), 1703–1712, doi:10.1016/j.buildenv.2005.07.006, 2006.
- O’Keeffe, K. P., Anjomshoa, A., Strogatz, S. H., Santi, P. and Ratti, C.: Quantifying the sensing power of vehicle fleets, *Proc. Natl. Acad. Sci. U. S. A.*, 116(26), 12752–12757, doi:10.1073/pnas.1821667116, 2019.
- Pan, L., Yao, E. and Yang, Y.: Impact analysis of traffic-related air pollution based on real-time traffic and basic meteorological information, *J. Environ. Manage.*, doi:10.1016/j.jenvman.2016.09.010, 2016.
- Righi, S., Lucialli, P. and Pollini, E.: Statistical and diagnostic evaluation of the ADMS-Urban model compared with an urban air quality monitoring network, *Atmos. Environ.*, 43(25), 3850–3857, doi:10.1016/j.atmosenv.2009.05.016, 2009.
- Rood, A. S.: Performance evaluation of AERMOD, CALPUFF, and legacy air dispersion models using the Winter Validation Tracer Study dataset, *Atmos. Environ.*, 89, 707–720, doi:10.1016/j.atmosenv.2014.02.054, 2014.
- Sanchez, B., Martilli, A., Palacios, M. and Kirchner, F.: CFD Modeling of Reactive Pollutants in an Urban Street Canyon using Different Chemical Mechanisms, (2), 1–6, 2005.
- Silva, B. N., Khan, M. and Han, K.: Towards sustainable smart cities: A review of trends, architectures, components, and open challenges in smart cities, *Sustain. Cities Soc.*, doi:10.1016/j.scs.2018.01.053, 2018.
- Solazzo, E., Vardoulakis, S. and Cai, X.: A novel methodology for interpreting air quality measurements from urban streets using CFD modelling, *Atmos. Environ.*, 45(29), 5230–5239, doi:10.1016/j.atmosenv.2011.05.022, 2011.
- Steffens, J. T., Heist, D. K., Perry, S. G., Isakov, V., Baldauf, R. W. and Zhang, K. M.: Effects of roadway configurations on near-road air quality and the implications on roadway designs, *Atmos. Environ.*, doi:10.1016/j.atmosenv.2014.05.015, 2014.
- Sun, J., Lenschow, D. H., LeMone, M. A. and Mahrt, L.: The Role of Large-Coherent-Eddy Transport in the Atmospheric Surface Layer Based on CASES-99 Observations, *Boundary-Layer Meteorol.*, doi:10.1007/s10546-016-0134-0, 2016.
- The PALM Group: The PALM model system, [online] Available from: <https://palm.muk.uni-hannover.de/trac>, 2020.
- The World Bank: Urban population, [online] Available from: <https://data.worldbank.org/indicator/SP.URB.TOTL.IN.ZS>, 2020.
- US EPA: Air Quality Dispersion Modeling - Preferred and Recommended Models, [online] Available from: <https://www.epa.gov/scram/air-quality-dispersion-modeling-preferred-and-recommended-models>, 2020.
- Vos, P. E. J., Maiheu, B., Vankerkom, J. and Janssen, S.: Improving local air quality in cities: To tree or not to tree?, *Environ. Pollut.*, 183, 113–122, doi:10.1016/j.envpol.2012.10.021, 2013.
- Wang, S., Ma, Y., Wang, Z., Wang, L., Chi, X., Ding, A., Yao, M., Li, Y., Li, Q., Wu, M., Zhang, L., Xiao, Y. and Zhang, Y.: Mobile monitoring of urban air quality at high spatial resolution by low-cost sensors: Impacts of COVID-19 pandemic lockdown, *Atmos. Chem. Phys. Discuss.*, 2020.
- WHO: WHO Global Urban Ambient Air Pollution Database, [online] Available from: https://www.who.int/phe/health_topics/outdoorair/databases/cities/en/, 2016.
- Wicker, L. J. and Skamarock, W. C.: Time-splitting methods for elastic models using forward time schemes, *Mon. Weather Rev.*, 130(8), 2088–2097, doi:10.1175/1520-0493(2002)130<2088:TSMFEM>2.0.CO;2, 2002.
- Wolf, T. and Esau, I.: A proxy for air quality hazards under present and future climate conditions in Bergen, Norway, *Urban Clim.*, 10(1), 801–814, doi:10.1016/j.uclim.2014.10.006, 2014.
- Wolf, T., Pettersson, L. H. and Esau, I.: A very high-resolution assessment and modelling of urban air quality, *Atmos. Chem. Phys.*, 20(2), 625–647, doi:10.5194/acp-20-625-2020, 2020.

- Yu, H. and Thé, J.: Simulation of gaseous pollutant dispersion around an isolated building using the $k-\Omega$ SST (shear stress transport) turbulence model, *J. Air Waste Manag. Assoc.*, 67(5), 517–536, doi:10.1080/10962247.2016.1232667, 2017.
- 580 Zhang, Y., Tao, S., Shen, H., Jianmin, M. and Ma, J.: Inhalation exposure to ambient polycyclic aromatic hydrocarbons and lung cancer risk of Chinese population, *Proc. Natl. Acad. Sci. U. S. A.*, 106(50), 21063–21067, doi:10.1073/pnas.0905756106, 2009.
- 585 Zhao, Y., Qiu, L. P., Xu, R. Y., Xie, F. J., Zhang, Q., Yu, Y. Y., Nielsen, C. P., Qin, H. X., Wang, H. K., Wu, X. C., Li, W. Q. and Zhang, J.: Advantages of a city-scale emission inventory for urban air quality research and policy: The case of Nanjing, a typical industrial city in the Yangtze River Delta, China, *Atmos. Chem. Phys.*, 15(21), 12623–12644, doi:10.5194/acp-15-12623-2015, 2015.
- Zheng, J., Che, W., Wang, X., Louie, P. and Zhong, L.: Road-network-based spatial allocation of on-road mobile source emissions in the pearl river delta region, China, and comparisons with population-based approach, *J. Air Waste Manag. Assoc.*, doi:10.3155/1047-3289.59.12.1405, 2009.
- 590 Zhong, J., Cai, X. M. and Bloss, W. J.: Modelling the dispersion and transport of reactive pollutants in a deep urban street canyon: Using large-eddy simulation, *Environ. Pollut.*, 200(September 2016), 42–52, doi:10.1016/j.envpol.2015.02.009, 2015.